








Cometary Activity Discovered on a Distant Centaur: A Nonaqueous Sublimation Mechanism

Colin Orion Chandler¹ , Jay K. Kueny^{1,2} , Chadwick A. Trujillo¹ , David E. Trilling¹ , and William J. Oldroyd¹ 

¹Department of Physics & Astronomy, Northern Arizona University, P.O. Box 6010, Flagstaff, AZ 86011, USA; Orion@nau.edu

²Lowell Observatory, 1400 W Mars Hill Rd, Flagstaff, AZ 86001, USA

Received 2020 January 23; revised 2020 February 25; accepted 2020 March 8; published 2020 April 6

Abstract

Centaur are minor planets thought to have originated in the outer solar system region known as the Kuiper Belt. Active Centaurs enigmatically display comet-like features (e.g., tails, comae) even though they orbit in the gas giant region where it is too cold for water to readily sublimate. Only 18 active Centaurs have been identified since 1927 and, consequently, the underlying activity mechanism(s) have remained largely unknown up to this point. Here we report the discovery of activity emanating from Centaur 2014 OG₃₉₂, based on archival images we uncovered plus our own new observational evidence acquired with the Dark Energy Camera (Cerro Tololo Inter-American Observatory Blanco 4 m telescope), the Inamori-Magellan Areal Camera & Spectrograph (Las Campanas Observatory 6.5 m Walter Baade Telescope), and the Large Monolithic Imager (Lowell Observatory 4.3 m Discovery Channel Telescope). We detect a coma as far as 400,000 km from 2014 OG₃₉₂, and our novel analysis of sublimation processes and dynamical lifetime suggest carbon dioxide and/or ammonia are the most likely candidates for causing activity on this and other active Centaurs. We find 2014 OG₃₉₂ is optically red, but CO₂ and NH₃ are spectrally neutral in this wavelength regime so the reddening agent is as yet unidentified.

Unified Astronomy Thesaurus concepts: Centaurs (215); Comae (271); Comet tails (274); Astrochemistry (75)

1. Introduction

Prior to the mid-20th century, comets were thought to be the only astronomical objects with tails or comae. Unsurprisingly, then, the first two active Centaur discoveries—29P/Schwassman–Wachmann 1 (Schwassmann & Wachmann 1927) and 39P/Oterma (Oterma 1942)—were initially classified as comets.

In 1949 the discovery of the first active asteroid, (4015) Wilson–Harrington (also designated 107P), blurred the dividing line between asteroid and comet (Cunningham 1950). In 1977 (2060) Chiron was discovered (Kowal & Gehrels 1977), the first member of the population now known as Centaurs. (2060) Chiron was later found to be active, making it the first object to be identified as a Centaur prior to activity discovery (Meech & Belton 1990).

We adopt the Centaur classification system (Jewitt 2009) that defines Centaurs as objects (1) with perihelia and semimajor axes between the orbits of Jupiter (~5 au) and Neptune (~30 au) and (2) not in 1:1 mean-motion resonance with a giant planet (as is the case for the Trojans). We distinguish between Centaurs and Jupiter-family comets (following Levison & Duncan 1994) via the Tisserand parameter with respect to Jupiter, given by

$$T_J = \frac{a_J}{a} + 2\sqrt{(1 - e^2)\frac{a}{a_J}} \cos(i), \quad (1)$$

with eccentricity e , inclination i , and the semimajor axes of the body and Jupiter a and a_J , respectively. Centaurs have $T_J \geq 3$, whereas Jupiter-family comets range between $2 < T_J < 3$.

Centaurs are thought to have migrated inward from the Kuiper Belt (see review by Morbidelli 2008), a region that

spans 30 au (Neptune’s orbital distance) to 50 au. Neptune Trojans may also serve as a Centaur reservoir (Horner & Lykawka 2010). Centaurs all orbit exterior to the 3 au water ice line so they cannot readily undergo sublimation. Surprisingly, though, 18 Centaurs (~4% of known Centaurs) have been found to display prominent comet-like features such as comae (e.g., Figure 1) or tails; these are the active Centaurs. Table 1 lists the known active Centaurs along with key physical parameters and discovery circumstances.

Our understanding of active Centaurs has been limited because of their faint apparent magnitudes (the mean apparent magnitude m_V at discovery is ~20; Table 1), since it is necessary to probe several magnitudes fainter in order to reliably detect activity via telescopic imaging. Spectroscopy has been used with some success to identify cometary activity originating from asteroids (Busarev et al. 2018), but this method requires even brighter targets than detection by imaging. Discovering activity on Centaurs is observationally challenging because they are faint, telescope time-intensive, and because they are rare. Active centaurs are discovered, on average, within ~10% of their perihelion distance (Table 1) where they are significantly brighter and, importantly, warmer.

Another significant obstacle to understanding active Centaurs stems from the extreme cold found at their orbital distances. Water and methanol ices have been detected on the surfaces of ~10 Centaurs, but only one of these, (2060) Chiron, has also been visibly active (see review; Peixinho et al. 2020). At surface temperatures less than 150 K and pressures below ~10⁻¹² bar many thermodynamical properties (e.g., enthalpy of sublimation) of volatile ices are not well known from laboratory experiments (Fray & Schmitt 2009). Moreover, ices may exist in two or more different structural forms; energy from the H₂O crystalline–amorphous state transition may even play a role in generating activity (Jewitt 2009).

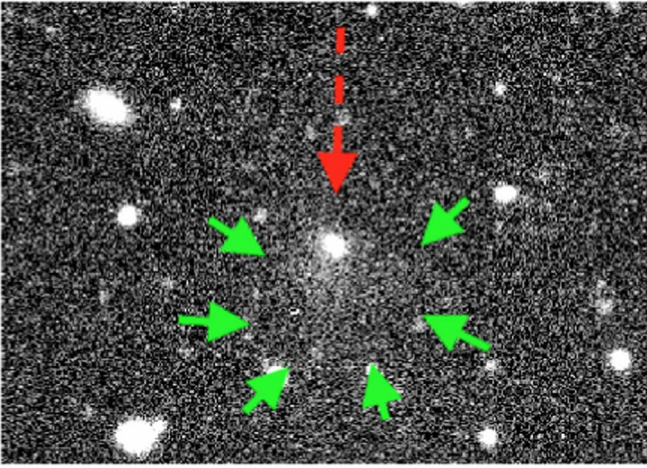


Figure 1. 2014 OG₃₉₂ (dashed arrow) displays a coma (short arrows) during our 2019 August 30 observations. Stack of 4×250 s DECam exposures.

2. Mining Archival Data

In order to overcome the observational challenges discussed in Section 1 we began by searching archival images captured with the 0.5 gigapixel Dark Energy Camera (DECam) on the Blanco 4 m telescope at the Cerro Tololo Inter-American Observatory in Chile. Archival data from this facility allow the detection of faint activity because of the relatively large aperture and because a large number of objects serendipitously imaged by the instrument can be searched.

We identified Centaurs in our own proprietary database cataloging the NSF’s National Optical-Infrared Astronomy Research Laboratory (NSF’s OIR Lab, formerly NOAO) public DECam archive following the methodology outlined in Chandler et al. (2018). Our general approach was to correlate image celestial coordinate and temporal data with object ephemeris services such as NASA JPL Horizons (Giorgini et al. 1996) and IMCCE SkyBot (Berthier et al. 2006; see also the acknowledgments).

We (1) extracted event information from the entire DECam public archive database, (2) submitted objects to SkyBot or matched against ephemerides produced via the Minor Planet Center and/or Horizons, and then (3) carried out a database query to identify potential images containing Centaurs.

After (4) downloading the data, we (5) checked each chip for the presence of the Centaur to ensure the object was visible and free of imaging complications (e.g., gaps between chips, scattered light from bright stars, cosmic rays). Finally, we (6) adhered to the routine outlined in Chandler et al. (2018) where, following image file retrieval of 2014 OG₃₉₂ from the archive, we extracted Flexible Image Transport System (FITS) and Portable Network Graphics (PNG) thumbnails (480×480 pixel images). We subjected these thumbnails to image processing techniques in order to assist by-eye analysis.

While examining each Centaur PNG thumbnail image by eye we flagged any with apparent activity for later analysis. FITS thumbnail images corresponding to those flagged were subjected to additional image processing techniques in an effort to enhance image quality, especially comae contrast.

To ascertain potential heliocentric distance effects we made use of a simple metric (Chandler et al. 2018), $\%_{T \rightarrow q}$, which describes how close to perihelion (q) an object’s distance (d) is

relative to its aphelion distance (Q):

$$\%_{T \rightarrow q} = \left(\frac{Q - d}{Q - q} \right) \cdot 100\%. \quad (2)$$

From DECam archival data we extracted ~ 20 thumbnail images of 2014 OG₃₉₂; Figure 2 shows the number of thumbnails obtained along with the predicted apparent V -band magnitude and observability of 2014 OG₃₉₂. In images from 2017 July and August, we spotted what appeared to be activity emanating from 2014 OG₃₉₂ (see gallery; Appendix B); at that time the object was 10.60 au from the Sun.

3. Follow-up Observing

To confirm the presence of activity we used the same DECam instrument and made additional observations on UT 2019 August 30. Figure 1 shows 2014 OG₃₉₂ with a telltale coma revealed by a combined 1000 s exposure. Appendix B contains a gallery showing the four constituent 250 s DECam exposures, plus two images where isophotal contours were overplotted to help identify coma extent for each of the first two exposures (Appendix B).

We made use of three observatories for follow-up observations of 2014 OG₃₉₂: (1) NSF’s OIR Labs DECam with VR filter on the Blanco 4 m telescope at the Cerro Tololo Inter-American Observatory in Chile (2) WB4800-7800 filtered imaging with the Magellan 6.5 m Walter Baade Telescope equipped with the Inamori-Magellan Areal Camera & Spectrograph (IMACS) at the Las Campanas Observatory on Cerro Manqui, Chile, and (3) g , r , and i filter images taken with the Large Monolithic Imager (LMI) at the Lowell Observatory 4.3 m Discovery Channel Telescope (DCT) in Arizona, USA. Galleries showing our Magellan images and DCT images are shown in Appendices B.4 and B.5, respectively. A log of observations is provided in Appendix A. Astrometric calibration was performed using the *astrometry.net* (Lang et al. 2010) and/or *PhotometryPipeline* (Mommert 2017) software packages.

4. Simulating Dynamical Lifetime

Determining the total mass loss possible for different volatiles requires knowledge of the dynamical lifetime of 2014 OG₃₉₂ in the Centaur region (where both perihelion distance and semimajor axis are between 5 and 30 au). To this end we made use of the REBOUND N -body integrator to model the orbits of 2014 OG₃₉₂ and giant planets Jupiter, Saturn, Uranus, and Neptune (Rein et al. 2019). We also carried out 25 simulations of 2014 OG₃₉₂, each with an orbital clone derived from the orbital uncertainties published by the Minor Planet Center. From these dynamical integrations, we found that the lifetime of 2014 OG₃₉₂ spans the range of 13,000–1.8 million years, roughly in agreement with prior work (Liu & Ip 2019).

5. Sublimation Modeling

In order to better assess potential processes responsible for 2014 OG₃₉₂ activity, we computed equilibrium temperatures and modeled mass-loss rates for seven astrophysically relevant ices: ammonia (NH_3), carbon dioxide (CO_2), carbon monoxide (CO), methane (CH_4), methanol (CH_3OH), nitrogen (N_2), and water (H_2O).

Table 1
Active Centaurs

Object Name or Designation	Orbital Elements				Activity Discovery				Reference
	P (yr)	a (au)	q (au)	Q (au)	r (au)	$\%_{T \rightarrow q}$	M_V	Date (UT)	
Chiron (95P)	50.5	6.0	8.5	18.9	11.8	68	17.0	1989 Apr 10	1
Echeclus (174P)	35.3	10.8	5.9	15.6	13.1	25	21.1	2005 Dec 4	2
29P/Schwassmann–Wachmann 1	14.8	6.0	5.5 ^a	6.6	6.0	53	15.3	1927 Nov 15	3
39P/Oterma	19.5	7.2	3.4 ^a	9.0	3.5	99	15.1	1942 Feb 12	4
165P/LINEAR	76.4	18.0	6.8	29.3	6.9	100	19.4	2000 Jan 9	5
166P/NEAT	51.9	13.9	8.6	19.2	8.6	100	19.6	2001 Oct 15	6
167P/CINEOS	64.8	16.1	11.8	20.5	12.2	96	20.7	2004 Jun 7	7
P/2005 S2 (Skiff)	22.5	8.0	6.4	9.5	6.5	98	19.7	2005 Sep 16	8
P/2005 T ₃ (Read)	20.6	7.5	6.2	8.8	6.2	100	20.7	2005 Oct 7	9
P/2011 C2 (Gibbs)	20.0	7.4	5.4	9.3	5.5	97	20.3	2011 Feb 12	10
C/2011 P2 (PanSTARRS)	30.6	9.8	6.2	13.4	6.3	98	20.3	2011 Aug 3	11
P/2011 S1 (Gibbs)	25.4	8.6	6.9	10.4	7.5	82	21.0	2011 Sep 18	12
C/2013 C2 (Tenagra)	64.4	16.1	9.1	23.0	9.8	96	19.1	2013 Feb 14	13
C/2013 P4 (PanSTARRS)	56.8	14.8	6.0	23.6	6.3	98	19.5	2013 Aug 15	14
P/2015 M2 (PanSTARRS)	19.3	7.2	5.9	8.5	5.9	100	19.5	2015 Jun 28	15
C/2015 T5 (Sheppard–Tholen)	147.9	28.0	9.3	46.6	9.4	100	22.3	2015 Oct 13	16
C/2016 Q4 (Kowalski)	69.0	16.8	7.1	26.5	7.5	98	20.1	2016 Aug 30	17
2003 QD ₁₁₂	82.8	19.0	7.9	30.1	12.7	57	21.7	2004 Oct 10	18
2014 OG ₃₉₂	42.5	12.2	10.0	14.4	10.6	86	21.1	2017 Jul 18	19

Notes. P : orbital period; a : semimajor axis; q : perihelion distance; Q : aphelion distance; r : heliocentric distance; $\%_{T \rightarrow q}$: fractional perihelion–aphelion distance (Equation (2)); M_V : apparent V-band magnitude. Q computed via $Q = a(1 + e)$ when otherwise unavailable. Asteroid parameters provided by the Minor Planet Center. Heliocentric distance and apparent magnitude courtesy of JPL Horizons (Giorgini et al. 1996).

^a Original value(s) from activity discovery epoch adopted where available; otherwise, values adopted from more recent epoch(s). Reference points to a source that discusses activity of the object.

References. 1: Meech & Belton (1990), 2: Choi et al. (2006), 3: Schwassmann & Wachmann (1927), 4: Oterma (1942), 5: Kusnirak & Balam (2000), 6: Pravdo et al. (2001), 7: Romanishin et al. (2004), 8: Gajdos et al. (2005), 9: Read & Scotti (2005), 10: Gibbs et al. (2011a), 11: Wainscoat et al. (2011), 12: Gibbs et al. (2011b), 13: Holvorcem et al. (2013), 14: Wainscoat et al. (2013), 15: Bacci et al. (2015), 16: Tholen et al. (2015), 17: Kowalski et al. (2016), 18: Jewitt (2009), 19: this work.

Object distance is the primary factor in determining potential ice sublimation effects. We began with a simple sublimation model (Hsieh et al. 2015) well suited to gaining broad insight into the observed activity from 2014 OG₃₉₂; we expanded the procedure to apply more generally to other volatile ices. As we do not know the composition of 2014 OG₃₉₂ we cannot make use of a more comprehensive model that includes effects of, for example, porosity, tortuosity, or crystal structure (Schorghofer 2008). Moreover, 2014 OG₃₉₂ is undoubtedly not composed of a single ice, and mixtures of ices can exhibit behavior uncharacteristic for any lone constituent (Grundy & Stansberry 2000). For the limiting case of an inert graybody orbiting at a distance R from the Sun (measured in au)

$$\frac{F_{\odot}}{R^2}(1 - A) = \chi \epsilon \sigma T_{\text{eq}}^4, \quad (3)$$

where the fiducial solar flux F_{\odot} is 1360 W m^{-2} , A is the Bond albedo (we choose 0.1 as representative for Centaurs; Peixinho et al. 2020), ϵ is the infrared emissivity of the ice (set here as 0.9), T_{eq} is the equilibrium temperature of the body, and σ is the Stefan–Boltzmann constant ($5.670 \times 10^{-8} \text{ W m}^{-2} \text{ K}^{-4}$). Here χ is a factor that describes the rotational and axial tilt effects on how much flux is received from the Sun: $\chi = 1$ indicates the maximum heating scenario where the body is a “slab” facing the Sun at all times; $\chi = \pi$ describes a body that rotates quickly with no axial tilt with respect to the Sun; and $\chi = 4$, which we adopt here, is used for a fast-rotating (on the order of a few hours) isothermal body in thermodynamic

equilibrium. Here “fast-rotating” means that the rotation period of the object is short compared to the thermal wave propagation time (Schorghofer 2008; Hsieh et al. 2015).

We next consider an energy balance that incorporates sublimation in addition to blackbody radiation (Hsieh et al. 2015):

$$\frac{F_{\odot}}{R^2}(1 - A) = \chi [\epsilon \sigma T^4 + L f_D \dot{m}_S(T)], \quad (4)$$

where f_D is the “diffusion barrier factor” that describes how much emission is blocked by overlaying material (e.g., regolith), and L the latent heat of sublimation. The mass-loss rate $\dot{m}_S(T)$ is given by

$$\dot{m} = P_V(T) \sqrt{\frac{\mu}{2\pi kT}}, \quad (5)$$

with μ the SI mass of one molecule, and k the Boltzmann constant of $1.38069 \times 10^{-23} \text{ J K}^{-1}$. The vapor pressure (in Pa) of the substance can be related to temperature by the Clausius–Clapeyron relationship

$$P_V(T) = e_S \exp \left[\frac{\Delta H_{\text{subl}}}{R_g} \left(\frac{1}{T_{\text{triple}}} - \frac{1}{T} \right) \right], \quad (6)$$

in which e_S is the saturation vapor pressure (in Pa) of the substance at the triple-point temperature T_{triple} , ΔH_{subl} is the heat of sublimation of the substance (in kJ mol^{-1}), and R_g is the ideal gas constant ($8.341 \text{ J mol}^{-1} \text{ K}^{-1}$).

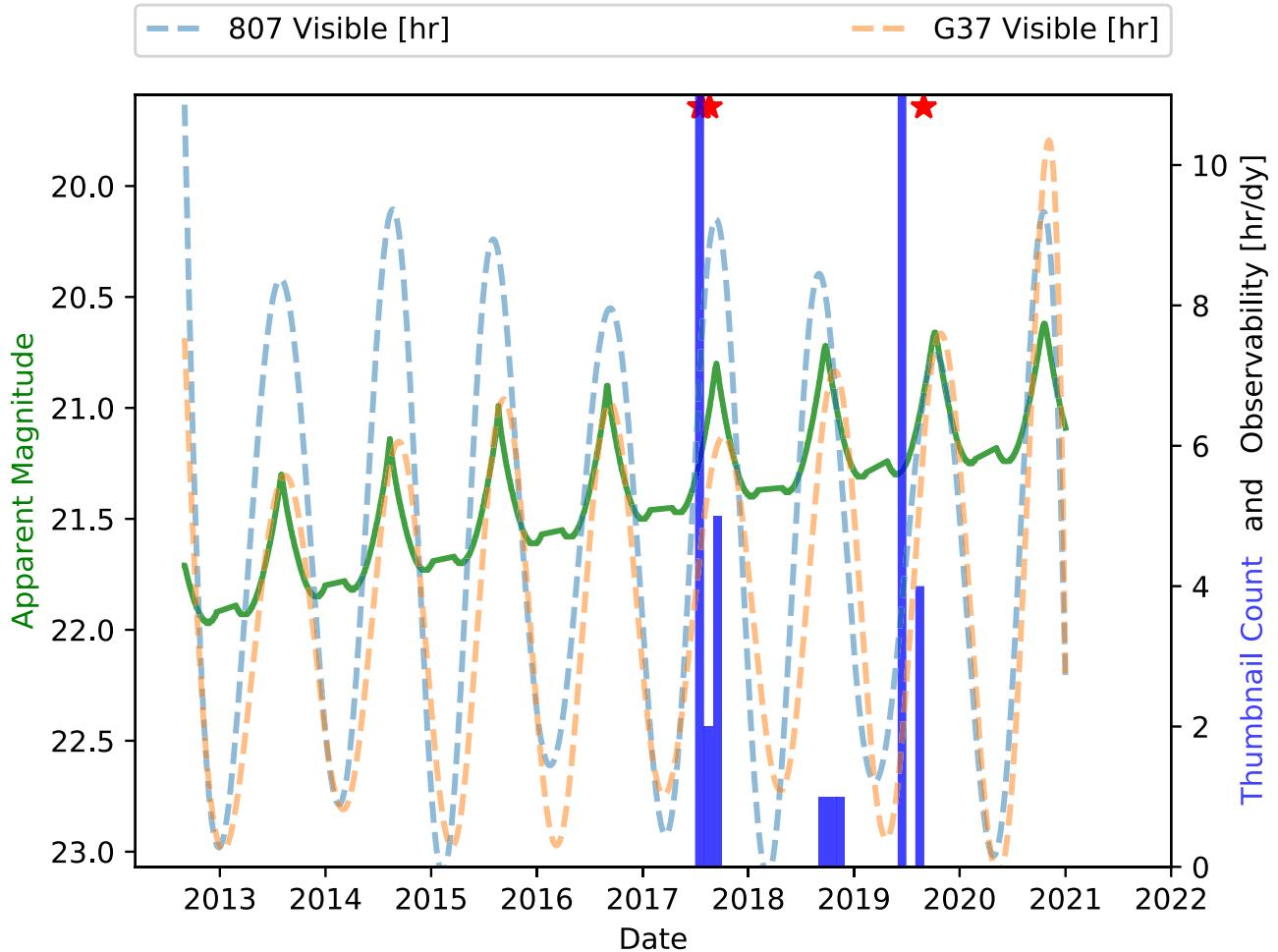


Figure 2. 2014 OG₃₉₂ activity timeline beginning 2012 September (DECam first light) to present. Red stars show when we found visible activity. The orbital period is ~ 42 yr so neither perihelion (2021 December 3) nor aphelion are visible on this plot. The solid green line (left vertical axis) shows the geocentric apparent V-band magnitude of 2014 OG₃₉₂. Dashed lines (right vertical axis) indicate the number of nighttime hours with elevation $>15^\circ$ for the southern hemisphere DECcam (blue; site code: 807) and for the northern hemisphere DCT (orange; site code: G37). The overlaid histogram (vertical blue bars and right axis) shows the number of thumbnail images captured during one calendar month. Note that in all instances when observability was high and many thumbnails were present, activity was observed.

Solving Equation (4) for heliocentric distance R (in au) yields

$$R(T) = \sqrt{\frac{F_\odot(1-A)}{\chi[\epsilon\sigma T^4 + L_{fD}\dot{m}_s(T)]}}. \quad (7)$$

Energy of sublimation values (Luna et al. 2014) and triple-point temperatures and pressures (Fray & Schmitt 2009) were incorporated as needed. To validate our model we computed the mass-loss rate for (2060) Chiron assuming $\chi = 4$, an albedo of 0.057, a diameter of 206 km, and an orbit ranging from 8.47 au at perihelion to 18.87 au at aphelion. Our (2060) Chiron model validation results were in rough agreement with the $0.5\text{--}20 \text{ kg s}^{-1}$ mass-loss rate reported by Womack et al. (2017).

We use our computed dynamical lifetime to circumstantially constrain the molecule(s) responsible for the sublimation of 2014 OG₃₉₂. Figure 3 shows, over the orbit of 2014 OG₃₉₂, the mass-loss rates for the different ices determined via modeling and validated through laboratory measurements. If 2014 OG₃₉₂ has an albedo of 10%, similar to that measured for other Centaurs (see review; Peixinho et al. 2020), then the body is about 20 km in diameter (see Section 7). Assuming a spherical

body of low density in the range of $1\text{--}3 \text{ g cm}^{-3}$ suggests a reasonable body mass of $(4.2\text{--}12.6) \times 10^{15} \text{ kg}$ and a surface area of $3.1 \times 10^8 \text{ m}^2$. Thus, the 13,000–1.8 Myr dynamical lifetime of 2014 OG₃₉₂ suggests a maximum orbit-averaged mass-loss rate in the range of $7.1 \times 10^{-7}\text{--}3.3 \times 10^{-5} \text{ kg m}^{-2} \text{ s}^{-1}$ (horizontal dashed lines in Figure 3) before the body would be entirely lost due to sublimation.

6. Colors

The archival data and our confirmation observations did not contain enough information to determine colors, so we obtained six 300 s exposures of 2014 OG₃₉₂ in a $g\text{--}r\text{--}i$ filter sequence at the DCT (Section 3). We made use of the *PhotometryPipeline* software package (Mommert 2017) to automate astrometry using SCAMP (Bertin 2006), which made use of the Vizier catalog service (Ochsenbein et al. 2000), Gaia Data Release 2 catalog (Gaia Collaboration et al. 2018), and photometric image calibration using solar stars from the Sloan Digital Sky Survey Data Release 9 (SDSS-DR9) catalog (Ahn et al. 2012). We carried out manual aperture photometry using the Aperture Photometry Tool (Laher et al. 2012).

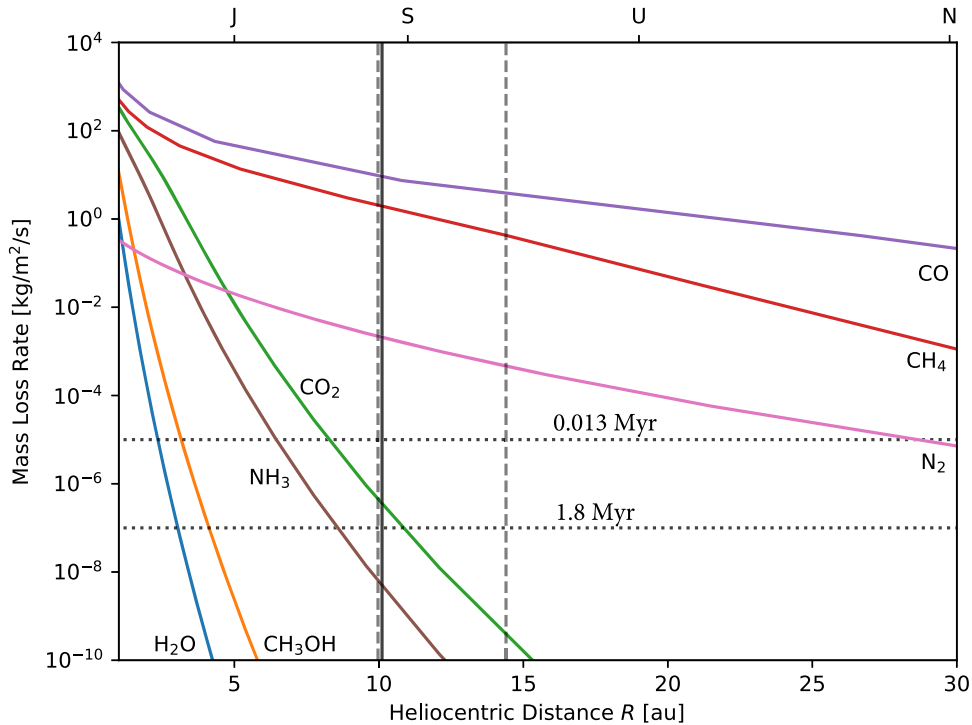


Figure 3. Mass-loss rates for seven different astrophysically relevant ices on an isothermal ($\chi = 4$) body; water (H_2O) and methanol (CH_3OH) ices have been detected on Centaurs. Orbital distances of Jupiter, Saturn, Uranus, and Neptune are indicated about the top axis. The current 10.11 au heliocentric distance of 2014 OG₃₉₂ is indicated by a vertical black bar, bracketed by perihelion (9.97 au) and aphelion (14.40 au) distances (leftmost and rightmost dashed vertical lines, respectively). Over the course of one orbit (between the vertical dashed lines), water and methanol never appreciably sublimate and carbon monoxide (CO), methane (CH_4), and molecular nitrogen (N_2) sublimate at high and relatively constant rates; we rule out all of these molecules as potential causes of activity. (The shallow slopes of CO, CH_4 , and N_2 extend beyond 50 au [not shown], which informs us the mass loss would have begun long before 2014 OG₃₉₂ became a Centaur.) However, over the course of one orbit the sublimation rates for CO_2 and NH_3 vary substantially, presumably producing significant variation in visible activity. Order-of-magnitude estimates of mass-loss-rate upper limits for the dynamical lifetime of 2014 OG₃₉₂ are shown as horizontal dotted lines. Only CO_2 and NH_3 have sublimation rates near these limits.

Prior to analysis we examined all thumbnail images showing activity emanating from 2014 OG₃₉₂ to ensure no significant background sources were blended with the nucleus. To help us identify unseen contaminators we measured and modeled surface brightness radial profiles of 2014 OG₃₉₂ (Figure 4) and a nearby solar-type star, using the Aperture Photometry Tool. The radial profile itself (i.e., not the model) was used to identify flux contribution by unseen background sources; we rejected images in which the nucleus or nearby coma was significantly contaminated. We note that we identified at least one background source within the coma in all of our images, although for color measurement we were able to use an aperture small enough (5 pixel radius) to exclude all resolvable background objects.

We measured 2014 OG₃₉₂ apparent magnitudes to be $g = 21.99 \pm 0.018$, $r = 21.19 \pm 0.016$, and $i = 20.81 \pm 0.018$. We compared our colors of $g - r = 0.80 \pm 0.024$ and $r - i = 0.39 \pm 0.024$ to SDSS reported solar colors of $g - r = 0.44 \pm 0.02$ and $r - i = 0.11 \pm 0.02$.³ Centaur colors are often reported in Johnson $B - R$ colors (see, e.g., Tegler et al. 2016), so we computed the $B - R$ color for 2014 OG₃₉₂ via Jester et al. (2005) transformations. We found $B - R = 1.64 \pm 0.4$, which is about one magnitude redder than the Sun, and red according to the classification system of Tegler et al. (2016) (see discussion in Section 9).

³ <http://www.sdss.org/dr12/algorithms/ugrizvegason>

7. Absolute Magnitude and Diameter Estimation

To gauge the overall spatial extent of the coma we examined the radial surface brightness profiles of 2014 OG₃₉₂ and nearby solar-type star J004840.66-022335.6 (see Section 6). We fit the profiles to the model

$$S(r) = A + Br + Cr^2 + Dr^3 + Er^4 + Fe^{-\frac{r^2}{2\sigma^2}} \quad (8)$$

as described in Gwyn et al. (2012).

After subtracting the sky flux from each profile and each model we scaled the star to the peak flux of the 2014 OG₃₉₂ radial profile. Figure 4 shows the radial profiles and their corresponding models plotted; we estimate the coma returns to sky background flux levels at ~ 60 pixels from the aperture center, thus the coma extent is $\sim 4.3 \times 10^5$ km. The FWHM of 2014 OG₃₉₂ was 13.62 ± 0.37 pixels ($3.2 \pm 0''.09$), whereas the star FWHM was 6.05 ± 0.05 pixels ($1.45 \pm 0''.012$).

As reported in Section 5, the coma is likely present throughout the orbit of 2014 OG₃₉₂. As a result, prior absolute (H) magnitude estimates would have included the excess flux caused by the coma, as evinced in Figure 4. To estimate the absolute nuclear magnitude of 2014 OG₃₉₂ we compared the ratio of the total (nucleus + coma) flux (blue line and circles, Figure 4) to the scaled stellar flux (orange line and triangles, Figure 4). We estimate the coma accounts for 0.75 and 1.1 magnitudes of the observed r -band and g -band fluxes, respectively, implying the nucleus apparent magnitudes are $m_r = 21.9$ and $m_g = 23.1$.

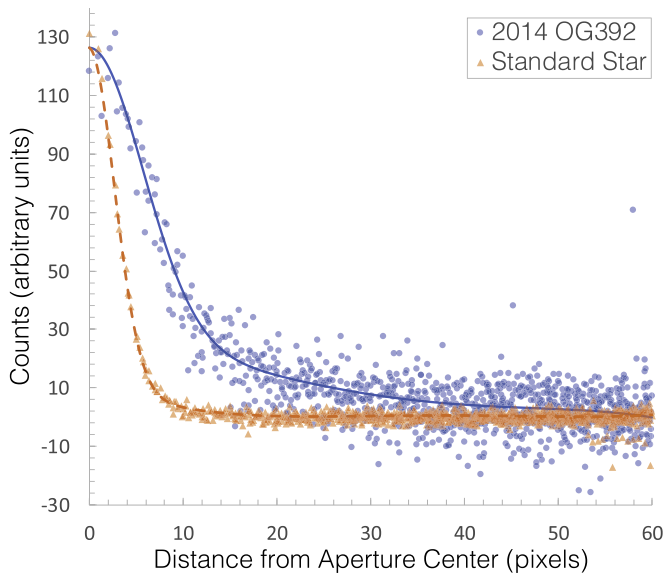


Figure 4. Surface brightness radial profiles of 2014 OG₃₉₂ and a nearby SDSS-DR9 catalog solar-type star (J004840.66-022335.6) are plotted along with a model fit for each object. After subtracting the background flux from the two profiles we normalized the standard star profile to the peak of the 2014 OG₃₉₂ profile. The coma flux tapers from 125 counts to background (0 counts) at $\rho \simeq 60$ pixels, or 4.3×10^5 km. We estimate there are $\sim 5.8 \times 10^{17}$ particles in the coma assuming a grain radius of 1 mm; for a density of 1 g cm^{-3} the total mass is 2.4×10^{15} g. Data from our 300 s *g*-band exposure taken on UT 2019 December 30 2:29 using the LMI on the Lowell Observatory 4.3 m DCT.

The absolute magnitude of an asteroid, H , is commonly used to estimate the size of small bodies in the solar system. H is defined as equal to the apparent V -band magnitude of an object observed at a heliocentric distance $R = 1$ au, a geocentric distance $\Delta = 1$ au, and a phase angle $\alpha = 0^\circ$. Here we employ the International Astronomical Union defined (Swings 1986) $H - G$ magnitude system approximated from Bowell et al. (1989):

$$V = 5 \log(R\Delta) + H - 2.5 \log[(1 - G)\Phi_1 + G\Phi_2], \quad (9)$$

where the phase function Φ is given by

$$\Phi_i = \exp[-A_i \tan(\alpha/2)^{B_i}]; \quad i = 1, 2 \quad (10)$$

with constants $A_1 = 3.33$, $A_2 = 1.87$, $B_1 = 0.63$, and $B_2 = 1.22$.

We make use of the relationships put forth by Jester et al. (2005) to derive Johnson $V = 22.4$ from our g and r nuclear magnitudes. The JPL Horizons ephemerides service (Giorgini et al. 1996) provided $G = 0.150$ (the standard assumed slope for dark surfaces), $r = 10.10$ au, $\Delta = 10.01$ au, and $\alpha = 5^\circ 58'$ for UT 2019 December 30. Via Equation (9) we find $H = 11.3$, 0.5 magnitudes fainter than reported by the Minor Planet Center and JPL Horizons.

Harris & Harris (1997) provide a convenient method to approximate object diameter D ,

$$D = \frac{1329}{\sqrt{G}} \times 10^{-H/5}, \quad (11)$$

which, for 2014 OG₃₉₂, gives $D \approx 20$ km.

8. Coma Dust Analysis

To facilitate comparing our 2014 OG₃₉₂ dust-related metrics with other works we adopt the instrument and

Table 2
Solar Apparent Magnitude by Filter

Filter	$m_{\odot,F}$
SDSS- <i>g</i>	-26.34
SDSS- <i>r</i>	-27.04
SDSS- <i>i</i>	-27.38

aperture-independent cometary dust production parameter described by A’Hearn et al. (1984). The metric, $Af\rho$ (units of cm), combines the mean albedo A of ejecta grains within an aperture of radius ρ (in cm), scaled by the filling factor f (unitless), which describes how much of the aperture area ($\pi\rho^2$) is filled by N grains of cross section area σ (in cm^2),

$$f = \frac{N(\rho)\sigma}{\pi\rho^2}. \quad (12)$$

We measured $Af\rho$ (following the method outlined by Shi et al. 2019) via

$$Af\rho = 4R^2\Delta^2 10^{0.4(m_{\odot,F} - m_{\text{OG},F})} \rho^{-1}, \quad (13)$$

where R is the 2014 OG₃₉₂ heliocentric distance in au, Δ is the geocentric distance of 2014 OG₃₉₂ in cm, and, for filter F , $m_{\odot,F}$ and $m_{\text{OG},F}$ are the magnitudes of the Sun and 2014 OG₃₉₂, respectively. For $m_{\odot,F}$ we made use of solar apparent Vega magnitudes⁴ (see Willmer 2018 for details) in Table 2.

To estimate the number of particles N within our measured $Af\rho$ we can substitute Equation (12) into the equality $Af\rho = Af\rho$,

$$Af\rho = A \frac{N(\rho)\sigma}{\pi\rho^2} \rho, \quad (14)$$

and solve for $N(\rho)$,

$$N(\rho) = Af\rho \frac{\pi\rho}{A\sigma}. \quad (15)$$

To quantify the total number of particles in the coma N_{tot} we can scale the aperture of Equation (15) to the 60 pixel aperture containing the entire coma, ρ_{max} ,

$$N(\rho_{\text{max}}) = Af\rho \frac{\pi\rho_{\text{max}}^2}{A\sigma\rho}. \quad (16)$$

Recall the quantity $Af\rho$, here, is a measured value, so the quantities $A\rho$ do not cancel in Equation (16).

Four of our observations, Images 15–18 (details in Appendix A) were suitable for directly measuring $Af\rho$. We found $Af\rho = 487 \pm 12$ cm with an aperture of 4.3×10^5 km. With the albedo adopted for our sublimation modeling ($A = 0.1$) and a 1 mm radius grain, the coma around 2014 OG₃₉₂ is composed of roughly 5.8×10^{17} particles. Assuming a grain density of 1 g cm^{-3} the total coma mass is $\sim 2.4 \times 10^{15}$ g.

9. Discussion

The activity we observed spans more than two years, which rules out impact-driven activity. We determined that the two ices previously detected on Centaurs, water and methanol, would not appreciably sublimate at any point in 2014 OG₃₉₂’s

⁴ <http://mips.as.arizona.edu/~cnaaw/sun.html>

orbit and so should still be present in solid form on the surface (Figure 3). Moreover, CO, N₂, and CH₄ are highly volatile and sublimate at temperatures low enough that their supply is likely depleted, though reservoirs could still be trapped below the surface. We reiterate our model encompasses single-species ices subjected to the thermodynamic conditions outlined in Section 5; heterogeneous ice environments may alter sublimation chemistry (see, e.g., Grundy & Stansberry 2000), as can single-species state transitions (e.g., energy released during crystallization of amorphous water ice; see, e.g., Jewitt 2009).

We find that the molecule(s) most likely to drive the observed activity is either CO₂ and/or possibly NH₃. Neither would have sublimated appreciably at Kuiper Belt distances prior to 2014 OG₃₉₂ becoming a Centaur. Interestingly, both of these substances sublimate at rates that vary by over two orders of magnitude over the course of a 2014 OG₃₉₂ orbit, peaking at perihelion. As a result we predict 2014 OG₃₉₂ will become less active post-perihelion. This further implies that all other active Centaurs should follow this trend, with peak sublimation near perihelion and a significant drop in outgassing for most of their orbits.

We determined 2014 OG₃₉₂ is at present roughly one magnitude redder than the Sun at visible wavelengths. However, we were only able to obtain two images in each filter, so uncertainty could be improved upon with additional observations. Our color measurements inexorably included the coma; future observations during a quiescent period (should one exist) would allow for color measurements of the bare nucleus. We did, however, attempt to better estimate the H magnitude by subtracting the coma measured in the radial surface brightness profiles. We found 2014 OG₃₉₂ has $H \approx 11.3$, 0.5 magnitudes fainter than previously reported. The H magnitude implies a radius of about 20 km when assuming a slope parameter $G = 0.15$ as is typical for a dark surface.

In our images of 2014 OG₃₉₂ background sources were typically present in the coma and/or blended with the nucleus, but from four images we were able to directly measure dust properties. Assuming a 10% albedo and a grain radius of 1 mm we estimate the coma contains roughly 5.8×10^{17} particles. If the grain density is 1 g cm^{-3} , the total mass is $\sim 2.4 \times 10^{15}$ g, or $\sim 0.01\%$ the total mass of 2014 OG₃₉₂. If the coma mass is indeed of this scale, 2014 OG₃₉₂ must be eroding very quickly, undergoing new activity, or the ejecta is accumulating faster than it is escaping. Our measured $Af\rho$ of 487 ± 12 cm is comparable to other Centaurs active at the same orbital distance as 2014 OG₃₉₂: C/2011 P2 (PANSTARRS) with $Af\rho = 161 \pm 4$ cm at ~ 9 au (Mazzotta Epifani et al. 2017), and for 166P (NEAT) $Af\rho = 288 \pm 19$ cm at ~ 12 au (Shi & Ma 2015).

Centaurs are sometimes classified as either gray or red depending on whether the object has a $B - R$ color closer to ~ 1.2 or ~ 1.7 , respectively (see Tegler et al. 2008 and Peixinho et al. 2020 reviews for in-depth discussions). We find our derived $B - R$ color of 1.64 ± 0.4 consistent with the red classification. Notably both molecules we find viable for sublimation are spectrally neutral in visible wavelengths so the reddening agent is as yet unidentified. 2014 OG₃₉₂ will remain observable through 2020 February and will again be observable beginning around 2020 August. We anticipate imaging and spectroscopy will yield further insight into the nature of these rare objects. We wish to emphasize further lab work is needed

to characterize sublimation processes of volatiles under low pressure and temperature regimes.

We thank Dr. Mark Jesus Mendoza Magbanua (University of California San Francisco) for his frequent and timely feedback on the project. J.K.K. acknowledges support from Northern Arizona University through a startup award administered by TD Robinson. Mark Loeffler (NAU) and Patrick Tribbett (NAU) helped us interpret lab results. Stephen Tegler (NAU) provided extensive insight into the nuances of Centaur colors. Kazuo Kinoshita provided cometary elements that saved us considerable time and energy. The authors express their gratitude to Mike Gowanlock (NAU), Cristina Thomas (NAU), and the Trilling Research Group (NAU), all of whom provided insights that substantially enhanced this work. Thank you to Stephen Kane (University of California Riverside), Dawn Gelino (NASA Exoplanet Science Institute at California Institute of Technology), and Jonathan Fortney (University of California Santa Cruz) for encouraging the authors to pursue this work. The unparalleled support provided by Monsoon cluster administrator Christopher Coffey (NAU) and his High Performance Computing Support team greatly facilitated the work presented here.

This material is based upon work supported by the National Science Foundation Graduate Research Fellowship Program under grant No. 2018258765. Any opinions, findings, and conclusions or recommendations expressed in this material are those of the author(s) and do not necessarily reflect the views of the National Science Foundation.

Computational analyses were carried out on Northern Arizona University's Monsoon computing cluster, funded by Arizona's Technology and Research Initiative Fund. This work was made possible in part through the State of Arizona Technology and Research Initiative Program.

This research used the facilities of the Canadian Astronomy Data Centre operated by the National Research Council of Canada with the support of the Canadian Space Agency. We also employed their solar system Object Search (Gwyn et al. 2012). This research has made use of data and/or services provided by the International Astronomical Union's Minor Planet Center. This research has made use of NASA's Astrophysics Data System. This research has made use of the The Institut de Mécanique Céleste et de Calcul des Éphémérides (IMCCE) SkyBoT Virtual Observatory tool (Berthier et al. 2006). Simulations in this Letter made use of the REBOUND code, which is freely available at <http://github.com/hannorein/rebound>. This work made use of the FTOOLS software package hosted by the NASA Goddard Flight Center High Energy Astrophysics Science Archive Research Center. This research has made use of SAO Image DS9, developed by Smithsonian Astrophysical Observatory (Joye & Mandel 2003). This work made use of the Lowell Observatory Asteroid Orbit Database *astorbDB* (Moskovitz et al. 2019). This work made use of the *astropy* software package (Astropy Collaboration et al. 2013).

This project used data obtained with the Dark Energy Camera (DECam), which was constructed by the Dark Energy Survey (DES) collaboration. Funding for the DES Projects has been provided by the U.S. Department of Energy, the U.S. National Science Foundation, the Ministry of Science and Education of Spain, the Science and Technology Facilities Council of the United Kingdom, the Higher Education Funding

Council for England, the National Center for Supercomputing Applications at the University of Illinois at Urbana-Champaign, the Kavli Institute of Cosmological Physics at the University of Chicago, Center for Cosmology and Astro-Particle Physics at the Ohio State University, the Mitchell Institute for Fundamental Physics and Astronomy at Texas A&M University, Financiadora de Estudos e Projetos, Fundação Carlos Chagas Filho de Amparo, Financiadora de Estudos e Projetos, Fundação Carlos Chagas Filho de Amparo à Pesquisa do Estado do Rio de Janeiro, Conselho Nacional de Desenvolvimento Científico e Tecnológico and the Ministério da Ciência, Tecnologia e Inovação, the Deutsche Forschungsgemeinschaft and the Collaborating Institutions in the Dark Energy Survey. The Collaborating Institutions are Argonne National Laboratory, the University of California at Santa Cruz, the University of Cambridge, Centro de Investigaciones Energéticas, Medioambientales y Tecnológicas–Madrid, the University of Chicago, University College London, the DES-Brazil Consortium, the University of Edinburgh, the Eidgenössische Technische Hochschule (ETH) Zürich, Fermi National Accelerator Laboratory, the University of Illinois at Urbana-Champaign, the Institut de Ciències de l’Espai (IEEC/CSIC), the Institut de Física d’Altes Energies, Lawrence Berkeley National Laboratory, the Ludwig-Maximilians Universität München and the associated Excellence Cluster Universe, the University of Michigan, NSF’s National Optical-Infrared Astronomy Research Laboratory, the University of Nottingham, the Ohio State University, the University of Pennsylvania, the University of Portsmouth, SLAC National Accelerator Laboratory, Stanford University, the University of Sussex, and Texas A&M University.

This work is based in part on observations at Cerro Tololo Inter-American Observatory, National Optical Astronomy Observatory (Prop. IDs 2019A-0337, PI: Trilling; 2014B-0404, PI: Schlegel), which is operated by the Association of Universities for Research in Astronomy (AURA) under a cooperative agreement with the National Science Foundation.

These results made use of the Discovery Channel Telescope at Lowell Observatory. Lowell is a private, non-profit institution dedicated to astrophysical research and public

appreciation of astronomy and operates the DCT in partnership with Boston University, the University of Maryland, the University of Toledo, Northern Arizona University and Yale University. The Large Monolithic Imager was built by Lowell Observatory using funds provided by the National Science Foundation (AST-1005313). This Letter includes data gathered with the 6.5 m Magellan Telescopes located at Las Campanas Observatory, Chile.

Appendix A Activity Observation Details

Table A1 provides a listing of the observations used in this work.

Table A1
Activity Observations

#	Instrument	Date/Time (UT)	Exp. (s)	Filter
1	DECam ^a	2017 Jul 18 09:27	137	<i>z</i>
2	DECam ^a	2017 Jul 18 10:20	250	<i>z</i>
3	DECam ^a	2017 Jul 22 05:37	79	<i>g</i>
4	DECam ^a	2017 Jul 25 06:25	60	<i>r</i>
5	DECam ^a	2017 Jul 25 06:32	52	<i>r</i>
6	DECam ^a	2017 Aug 20 04:48	67	<i>r</i>
7	DECam ^b	2019 Aug 30 09:54	250	<i>VR</i>
8	DECam ^b	2019 Aug 30 09:58	250	<i>VR</i>
9	DECam ^b	2019 Aug 30 10:03	250	<i>VR</i>
10	DECam ^b	2019 Aug 30 10:08	250	<i>VR</i>
11	IMACS	2019 Dec 27 00:54	300	WB4800-7800
12	IMACS	2019 Dec 27 01:01	300	WB4800-7800
13	IMACS	2019 Dec 27 01:36	600	WB4800-7800
14	LMI	2019 Dec 30 02:08	300	<i>g</i>
15	LMI	2019 Dec 30 02:17	300	<i>r</i>
16	LMI	2019 Dec 30 02:23	300	<i>i</i>
17	LMI	2019 Dec 30 02:29	300	<i>g</i>
18	LMI	2019 Dec 30 02:35	300	<i>r</i>
19	LMI	2019 Dec 30 02:41	300	<i>i</i>

Notes.

^a Program 2014B-0404 (PI: Schlegel).

^b Program 2019A-0337 (PI: Trilling).

Appendix B Thumbnail Gallery

Figure B1 shows six of the archival images in which we originally spotted what appeared to be activity emanating from 2014 OG₃₉₂. We obtained confirmation first through DECam observations (Figure B2); the coma is more readily apparent in the isophotal contours shown in Figure B3. Figure B4 shows two additional observations we took at Magellan provided additional confirmation. Figure B5 shows six images of 2014 OG₃₉₂ we captured at the DCT which enabled us to perform color measurement and radial surface brightness profiling.

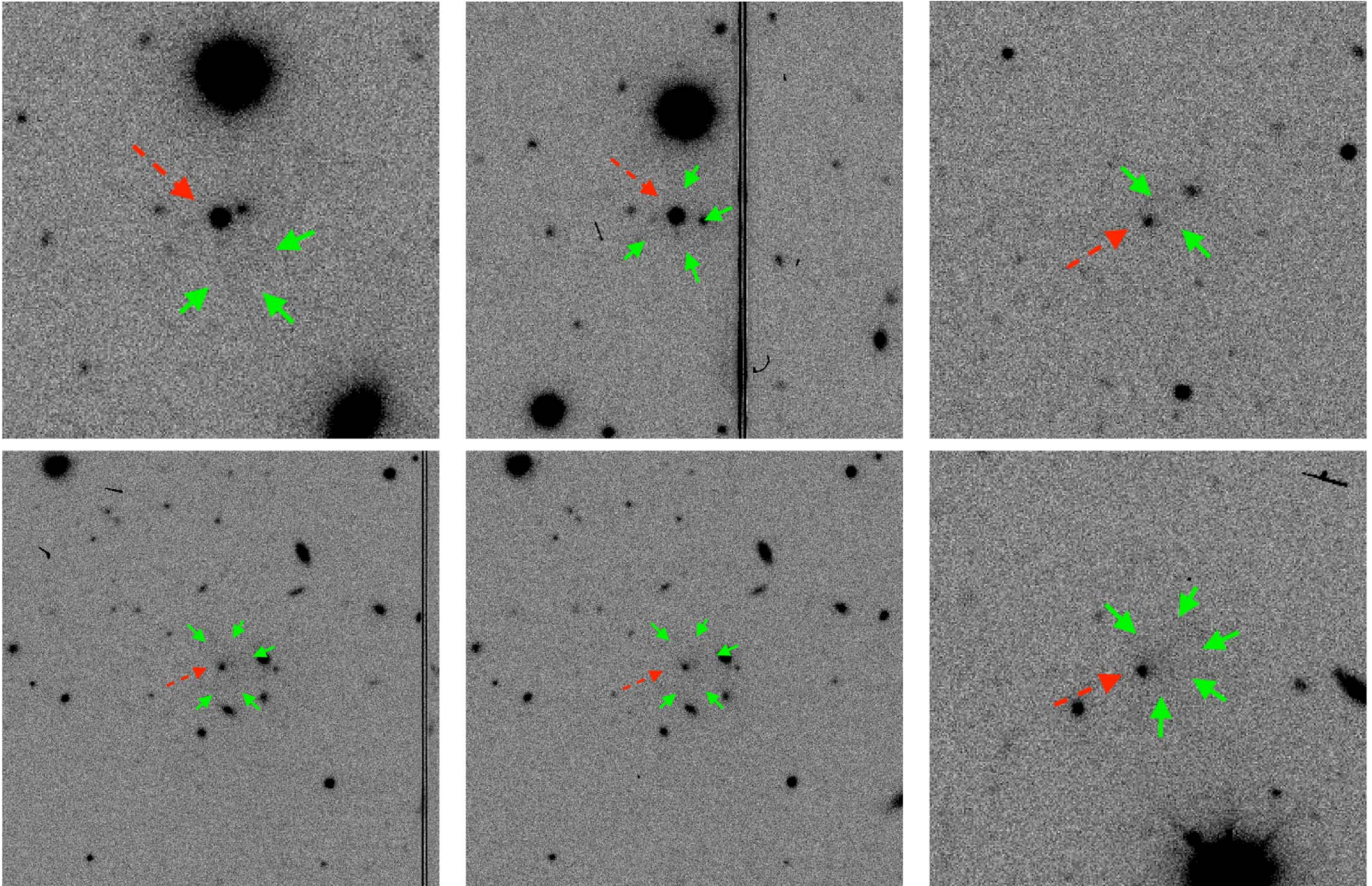


Figure B1. *DECam Archival Images.* Top left: UT 2017 July 18 09:27–137 s *z*-band. Top center: UT 2017 July 18 10:20–250 s *z*-band. Top right: UT 2017 July 22 05:37–79 s *g*-band. Bottom left: UT 2017 July 25 06:25–60 s *r*-band. Bottom center: UT 2017 July 25 06:32–52 s *r*-band. Bottom right: UT 2017 August 20 04:48–67 s *r*-band. All images: the coma (green arrows) was exceptionally faint in all of these DECam archival images of 2014 OG₃₉₂ (indicated by dashed red arrows), but nevertheless they prompted us to obtain follow-up observations.

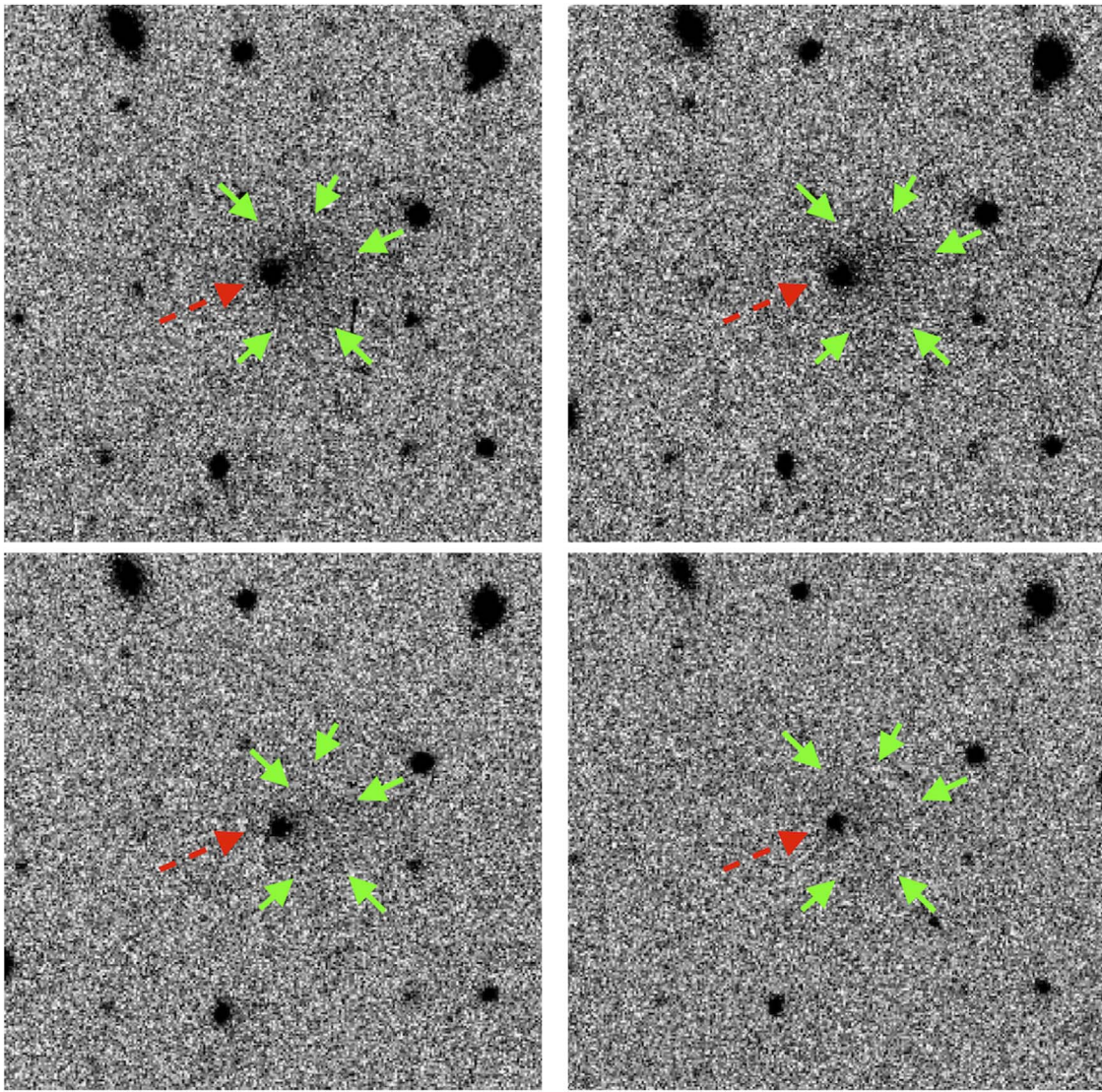


Figure B2. *New DECam Observations Gallery.* Top left: UT 9:54. Top right: UT 9:58. Bottom left: UT 10:03. Bottom right: UT 10:08. All images: (1) dashed red arrow points to 2014 OG₃₉₂, (2) green arrows highlight the comae if visible, (3) observing date was UT 2019 August 30, (4) filter was *VR*, and (5) exposure time was 250 s. The apparent decrease in coma prominence was the result of increasing background noise as images were taken into twilight.

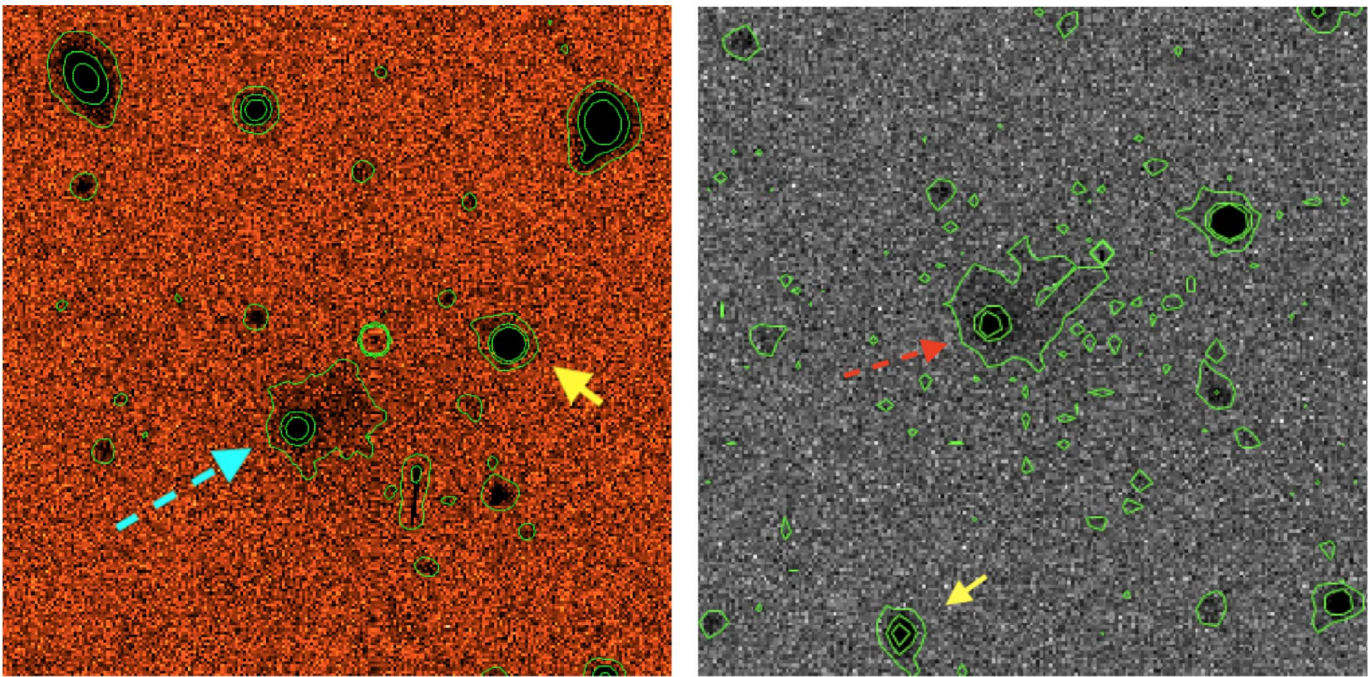


Figure B3. *Isophotal Contours Gallery.* Isophotal contours indicate the extent and irregularity of the coma emanating from 2014 OG₃₉₂ (dashed arrows), especially when contrasted with background objects (yellow arrows) presenting relatively symmetric radial profiles. These two 250 s VR-band exposures were taken at 9:54 (left) and 9:58 (right) during our UT 2019 August 30 follow-up campaign.

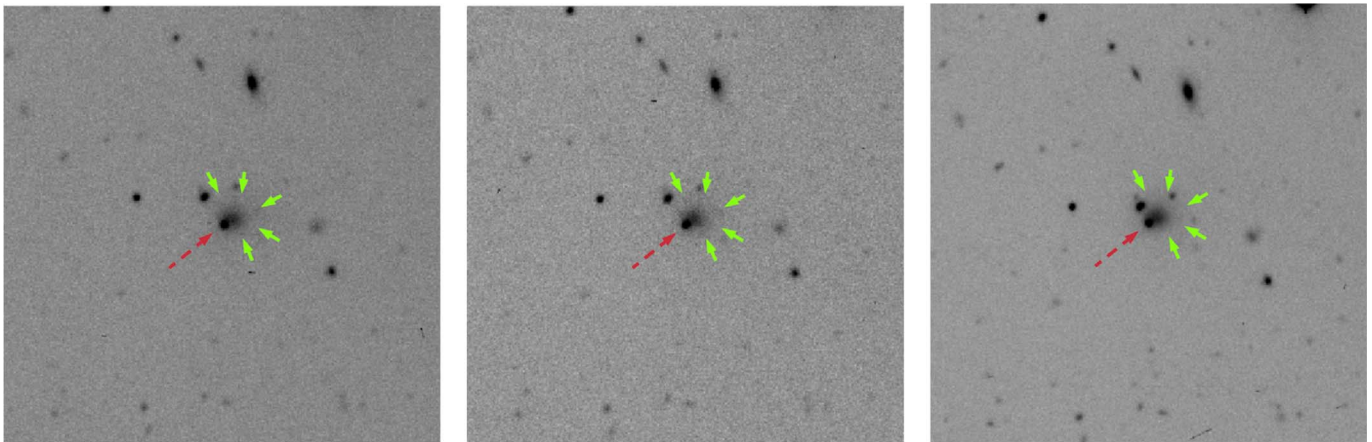


Figure B4. *New Magellan Observations Gallery.* 2014 OG₃₉₂ imaged 2019 December 27 via the Magellan 6.5 m Baade Telescope using the WB4800-7800 filter on the IMACS at Las Campanas Observatory on Cerro Manqui, Chile. The three images reveal an apparent coma (green arrows) emerging from the object (red dashed arrow) and were taken at 300 s (left and center) exposures and one 600 s exposure (right).

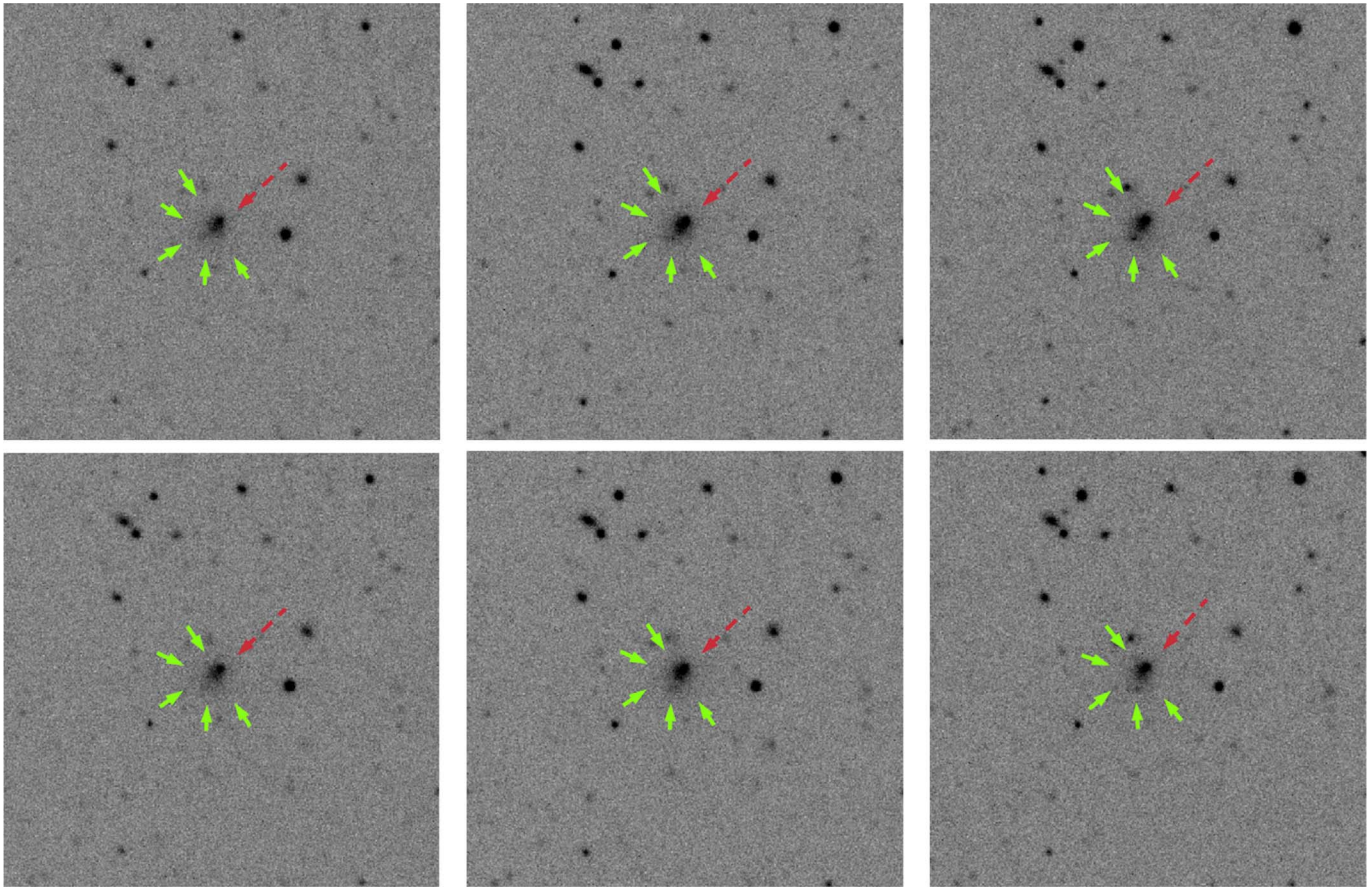


Figure B5. *New DCT Observations Gallery.* 2014 OG₃₉₂ imaged 2019 December 30, via the Lowell Observatory 4.3 m Discovery Channel Telescope (Arizona, USA) using the LMI. Green arrows trace out a diffuse coma and a dashed red arrow points to the nucleus in each of the six images. Each exposure in the two $g-r-i$ sequences (top and bottom rows) was 300 s long.

ORCID iDs

Colin Orion Chandler  <https://orcid.org/0000-0001-7335-1715>

Jay K. Kueny  <https://orcid.org/0000-0001-8531-038X>

Chadwick A. Trujillo  <https://orcid.org/0000-0001-9859-0894>

David E. Trilling  <https://orcid.org/0000-0003-4580-3790>

William J. Oldroyd  <https://orcid.org/0000-0001-5750-4953>

References

- A'Hearn, M. F., Schleicher, D. G., Millis, R. L., Feldman, P. D., & Thompson, D. T. 1984, *AJ*, **89**, 579
- Ahn, C. P., Alexandroff, R., Allende Prieto, C., et al. 2012, *ApJS*, **203**, 21
- Astropy Collaboration, Robitaille, T. P., Tollerud, E. J., et al. 2013, *A&A*, **558**, A33
- Bacci, P., Tesi, L., Fagioli, G., et al. 2015, MPEC, **2015-N46**, 1
- Berthier, J., Vachier, F., Thuillot, W., et al. 2006, in ASP Conf. Ser. 351, *SkyBoT, A New VO Service to Identify Solar System Objects*, ed. C. Gabriel et al. (San Francisco, CA: ASP), 367
- Bertin, E. 2006, in ASP Conf. Ser. 351, *Automatic Astrometric and Photometric Calibration with SCAMP*, ed. C. Gabriel (San Francisco, CA: ASP), 112
- Bowell, E., Hapke, B., Domingue, D., et al. 1989, in Conf. Proc. Asteroids II, ed. R. P. Binzel, T. Gehrels, & M. S. Matthews (Tucson, AZ: Univ. Arizona Press), 524
- Busarev, V. V., Makalkin, A. B., Vilas, F., Barabanov, S. I., & Scherbina, M. P. 2018, *Icar*, **304**, 83
- Chandler, C. O., Curtis, A. M., Mommert, M., Sheppard, S. S., & Trujillo, C. A. 2018, *PASP*, **130**, 114502
- Choi, Y. J., Weissman, P. R., & Polishook, D. 2006, *IAUC*, **8656**, 2
- Cunningham, L. E. 1950, *IAUC*, **1250**, 3
- Fray, N., & Schmitt, B. 2009, *P&SS*, **57**, 2053
- Gaia Collaboration, Brown, A. G. A., Vallenari, A., et al. 2018, *A&A*, **616**, A1
- Gajdos, S., Vilagi, J., Naves, R., et al. 2005, MPEC, **2005-T26**, 1
- Gibbs, A. R., Sarneczky, K., Scotti, J. V., et al. 2011a, *IAUC*, **9199**, 1
- Gibbs, A. R., Tornero, S. F., & Williams, G. V. 2011b, *IAUC*, **9234**, 1
- Giorgini, J. D., Yeomans, D. K., Chamberlin, A. B., et al. 1996, AAS/DPS Meeting Abstracts, **28**, 25.04
- Grundy, W. M., & Stansberry, J. A. 2000, *Icar*, **148**, 340
- Gwyn, S. D. J., Hill, N., & Kavelaars, J. J. 2012, *PASP*, **124**, 579
- Harris, A. W., & Harris, A. W. 1997, *Icar*, **126**, 450
- Holvorcem, P. R., Schwartz, M., Sato, H., Stevens, B. L., & Williams, G. V. 2013, *CBET*, **3417**, 1
- Horner, J., & Lykawka, P. S. 2010, *MNRAS*, **402**, 13
- Hsieh, H. H., Denneau, L., Wainscoat, R. J., et al. 2015, *Icar*, **248**, 289
- Jester, S., Schneider, D. P., Richards, G. T., et al. 2005, *AJ*, **130**, 873
- Jewitt, D. 2009, *AJ*, **137**, 4296
- Joye, W. A., & Mandel, E. 2003, in ASP Conf. Ser. 295, *New Features of SAOImage DS9*, ed. H. E. Payne, R. I. Jedrzejewski, & R. N. Hook (San Francisco, CA: ASP), 489
- Kowal, C. T., & Gehrels, T. 1977, *IAUC*, **3129**, 1
- Kowalski, R. A., Birtwhistle, P., Sato, H., et al. 2016, *CBET*, 4314
- Kusnirak, P., & Balam, D. 2000, *IAUC*, **7368**, 2
- Laher, R. R., Gorjian, V., Rebull, L. M., et al. 2012, *PASP*, **124**, 737
- Lang, D., Hogg, D. W., Mierle, K., Blanton, M., & Roweis, S. 2010, *AJ*, **139**, 1782
- Levison, H. F., & Duncan, M. J. 1994, *Icar*, **108**, 18
- Liu, P.-Y., & Ip, W.-H. 2019, *ApJ*, **880**, 71
- Luna, R., Satorre, M. Á., Santonja, C., & Domingo, M. 2014, *A&A*, **566**, A27
- Mazzotta Epifani, E., Perna, D., Dotto, E., et al. 2017, *A&A*, **597**, A59
- Meech, K. J., & Belton, M. J. S. 1990, *AJ*, **100**, 1323
- Mommert, M. 2017, *A&C*, **18**, 47

- Morbidelli, A. 2008, in *Trans-Neptunian Objects and Comets*. Saas-Fee Advanced Course 35, ed. D. Jewitt, A. Morbidelli, & H. Rauer (Berlin: Springer), 79
- Moskovitz, N., Schotland, R., Burt, B., et al. 2019, *EPSC*, 13, 644
- Ochsenbein, F., Bauer, P., & Marcout, J. 2000, *A&AS*, 143, 23
- Oterma, L. 1942, Bureau Central Astronomique de l'Union Astronomique Internationale, 900, 1
- Peixinho, N., Thirouin, A., Tegler, S. C., et al. 2020, in *The Trans-Neptunian Solar System*, ed. D. Prialnik, M. A. Barucci, & L. Young (New York: Elsevier), 307
- Pravdo, S., Helin, E. F., Hicks, M., & Lawrence, K. 2001, *IAUC*, 7738, 1
- Read, M. T., & Scotti, J. V. 2005, *IAUC*, 8614, 2
- Rein, H., Hernandez, D. M., Tamayo, D., et al. 2019, *MNRAS*, 485, 5490
- Romanishin, W., Tegler, S. C., Boattini, A., De Luise, F., & Di Paola, A. 2004, *IAUC*, 8545, 1
- Schorghofer, N. 2008, *ApJ*, 682, 697
- Schwassmann, A., & Wachmann, A. A. 1927, Bureau Central Astronomique de l'Union Astronomique Internationale Observatoire de Copenhague, 171, 1
- Shi, J., Ma, Y., Liang, H., & Xu, R. 2019, *NatSR*, 9, 5492
- Shi, J. C., & Ma, Y. H. 2015, *MNRAS*, 454, 3635
- Swings, J. P. 1986, *IAUTB*, 19, 1
- Tegler, S. C., Bauer, J. M., Romanishin, W., & Peixinho, N. 2008, in *The Solar System Beyond Neptune*, ed. M. A. Barucci et al. (Tucson, AZ: Univ. Arizona Press), 105
- Tegler, S. C., Romanishin, W., & Consolmagno, G. J., J. S. 2016, *AJ*, 152, 210
- Tholen, D. J., Trujillo, C., & Sheppard, S. S. 2015, *CBET*, 4177, 1
- Wainscoat, R., Denneau, L., Hsieh, H., et al. 2011, *IAUC*, 9225, 1
- Wainscoat, R., Veres, P., Micheli, M., et al. 2013, *CBET*, 3638, 1
- Willmer, C. N. A. 2018, *ApJS*, 236, 47
- Womack, M., Sarid, G., & Wierzbos, K. 2017, *PASP*, 129, 031001